Mechanisms for late 20th and early 21st Century decadal AMOC variability

Alex Megann, Adam Blaker, Simon Josey, Adrian New and Bablu Sinha

National Oceanography Centre, European Way, Southampton SO14 3ZH, UK

Contact address: apm@noc.ac.uk

Key points

- We use three ¼° forced NEMO integrations to investigate mechanisms for AMOC variability.
- Decadal AMOC variability is mainly forced by winter cooling in the Irminger Sea, and to a lesser extent by cooling in the Labrador Sea.
- An annual index, derived from the surface-forced streamfunction and accumulated over 10 years, has predictive skill for the AMOC strength.

Abstract

Recent studies, using data from the OSNAP observational campaign and from numerical ocean models, suggest that surface buoyancy losses over the Iceland Basin and the Irminger Sea may, in contradiction to the established consensus, be more significant than those over the Labrador Sea, and that these former regions are in fact the dominant sites for formation of upper North Atlantic Deep Water, with the Labrador Sea acting mainly as a region of further densification as the dense waters flow around the gyre. Here we present a set of hindcast integrations of a global 1/4° NEMO ocean configuration from 1958 until nearly the present day, forced with three standard surface forcing datasets. We use the surface-forced streamfunction, estimated from surface buoyancy fluxes, along with the overturning streamfunction, similarly defined in potential density space, to investigate the causal link between surface forcing and decadal variability in the strength of the Atlantic meridional overturning circulation (AMOC). A scalar metric based on the surface forced streamfunction, evaluated in critical density and latitude classes, and accumulated in time, is found to be a good predictor of changes in the overturning strength, and the surface heat loss from the Irminger Sea is confirmed to be the dominant mechanism for decadal AMOC variability. We use the streamfunctions to demonstrate that the watermasses in the simulations are transformed to higher densities as they propagate around the subpolar gyre from their formation locations in the north-east Atlantic and the Irminger Sea, consistent with the picture emerging from observations.

Plain Language Summary

The Atlantic Meridional Overturning Circulation (AMOC), which brings warm waters to the North Atlantic and warms the climate of northern Europe, is known to vary on timescales from annual to many centuries, with significant impacts on European climate. In this paper we use three numerical model integrations, linking decadal-timescale changes in the rate of formation of the

deep waters exported southwards to changes in the sea surface fields used to force the models. We show that AMOC variability is linked most strongly to wintertime cooling over the Irminger Sea, with cooling over the Labrador Sea having a smaller influence. Using the rates of density increase at each latitude due to surface buoyancy losses, accumulated over ten years, we create an annual index that follows the AMOC strength closely, and show that this has the potential to predict AMOC changes.

Keywords

North Atlantic; Decadal variability; Meridional overturning circulation; Surface buoyancy forcing

1. Introduction

The projections of the models included in the Coupled Model Intercomparison Project Phase 5 (CMIP5) indicate a reduction in the strength of the Atlantic meridional overturning circulation (AMOC) into the 21st Century as a result of anthropogenic greenhouse gas emissions (Cheng et al., 2013), leading to a substantial cooling over northern Europe resulting from the associated reduction in ocean heat transport (Liu et al., 2020). At the same time, variations occur on time scales from interannual to decadal, and these too have at least as strong an influence on European climate as the longer-term trends. In particular, AMOC variations are linked to multidecadal swings in the North Atlantic sea surface temperature index, the Atlantic Multidecadal Variability (AMV), with known impacts on the weather and climate (including temperature, rainfall, and hurricane activity) of the adjacent continents and further afield (see e.g., Sutton et al., 2018). Recent reports of an apparent decline in the AMOC have created more than a little interest, with a reduction of about 3 Sv at 26°N since 2008 being reported in the RAPID time series (Smeed et al., 2018), which is significantly more rapid than the projected decrease from increasing CO_2 concentrations. To place this variation in the context of longer timescales, estimates of the AMOC strength based on proxy data such as temperature and surface elevation have been used to extrapolate the AMOC strength before the RAPID era: Worthington et al. (2020) used the 26°N RAPID data to create an empirical model which they then applied to earlier hydrographic datasets, deriving an AMOC timeseries that has a maximum in the late 1990s, followed by a gradual reduction towards the start of the RAPID campaign in around 2005. Further back, less robust proxy data (e.g., Delworth et al., 2016) suggest that the AMOC gradually rose from the 1970s to the peak in the 1990s. There have been recent suggestions that the AMOC is currently in a recovery phase after the decline reported by Smeed et al. (2018) and others. The overturning and surface-forced indices derived by Desbruyères et al. (2019) from observational datasets show a decline of about 3 Sv from 1993 to 2010, followed by a sharp increase of about 4 Sv between 2010 and 2018, and Moat et al., (2020) use data from the RAPID array at to estimate a recovery of a similar magnitude over the same period.

The downwelling leg of the AMOC in the North Atlantic, driven by episodes of winter buoyancy loss at multiple locations in the subpolar gyre and the Nordic Seas, and leading to the production of southward-flowing North Atlantic Deep Water (NADW), has long been understood as a central control on the strength of the overturning circulation, and thence on the meridional ocean heat transport. Until the last decade, the consensus has been that this system was dominated by convection in the Labrador Sea and the Nordic Seas, with each contributing about half of the total volume of the NADW (e.g., Mauritzen, 1996, Schmitz & McCartney, 1993; Worthington, 1976), and analysis of numerical models (e.g., Bleck & Sun, 2004; Danabasoglu et al., 2012; Eden & Willebrand, 2001; Kuhlbrodt et al., 2007; and Roberts et al., 2013), reinforced this view.

Nevertheless, one or two authors questioned this hypothesis; for example, Pickart & Straneo (2003) suggested that "Labrador Sea Water", constituting the upper portion of NADW, was in fact mainly created in the Irminger and Iceland Basins, and over the past decade the prevailing consensus has been seriously challenged by the availability of more comprehensive observations (in particular the Overturning in the Subpolar North Atlantic Programme, OSNAP) and by improved numerical models. Lozier et al. (2019) and Zou & Lozier (2016) used OSNAP data and a numerical model study, respectively, to investigate the strength of the links between variability of the AMOC and variability in the rate of deep water production and export, and conclude that the bulk of watermass conversion and its variability occurs east of Cape Farewell (i.e., in the Irminger Basin), and that the Labrador Sea has a minimal contribution to the total overturning. Other studies have strengthened the argument: Chafik & Rossby (2019) use hydrographic data to estimate transports in density classes, suggesting that the Nordic Seas, rather than the Labrador Sea, are key to the state of the MOC; while Petit et al. (2020) conclude that the lower limb of the AMOC is primarily composed of waters formed in the Nordic Seas and Irminger and Iceland basins.

A number of the foregoing studies have related the variability in production rate of NADW, and hence that of the AMOC, to variability in surface buoyancy fluxes, the latter themselves reflecting climatic indexes, primarily the North Atlantic Oscillation (NAO). The interannual and interdecadal variability in the properties of upper NADW, estimated using up to 60 years of hydrographic data, have been linked to changes in the North Atlantic Oscillation (NAO) index (Curry et al. 1998; Kieke & Yashayaev 2015; Stramma et al. 2004), with positive phases of the NAO corresponding to periods of stronger NADW production. Josey et al. (2019) ascribed at least some of the interannual variability in Irminger Sea convection to intense cooling events traced to Greenland tip jets, the latter in turn related to the relative strengths of the East Atlantic Pattern (EAP) and the NAO.

The causes of the NAO changes which drive NADW production are still debated. A null hypothesis is that NAO variability is essentially random and internally generated in the atmosphere (e.g., the unforced coupled model study of Dong

and Sutton, 2005). However, there are hints in some coupled model studies that suggest a weak feedback from the ocean (Ortega et al. 2017) arising from the AMOC and subsequent subpolar SST response to the NAO. The possibility of oceanic feedbacks contributing to NAO trends is further evidenced by Peings and Magnusdottir (2014) using multidecadal atmospheric reanalysis, observed SST and forced atmosphere simulations. Additionally, a number of studies have argued that external forcing may force the NAO and hence the AMOC. Öttera et al. (2010) provide evidence that solar and volcanic forcing may influence NAO trends, whilst Menary et al. (2020) highlight the sensitivity of the AMOC to the balance between anthropogenic aerosol and greenhouse gas forcing. The mechanism whereby aerosol forcing impacts the AMOC is still unclear, but is likely to be related to its influence on atmospheric circulation (including the NAO) and turbulent heat air-sea buoyancy fluxes rather than a direct impact on incident shortwave radiation (e.g., Robson et al. 2016). The attribution of NAO variability external drivers and/or internal variability is further confounded by the "signal to noise problem" in climate models which operates at least up to decadal timescales and possibly longer (Smith et al., 2020). This means that climate models may underestimate the impact of external forcing or the magnitude predictable internally-generated variations, making it harder at present to understand the drivers of observed changes in the NAO such as the increasing trend seen between the 1960s and 1990s.

The representation of the meridional overturning circulation by a streamfunction in density coordinates, instead of the conventional fixed-depth coordinate, is more faithful to the tendency of watermasses to follow isopycnal surfaces rather than depth levels, and in particular avoids the aliasing of the gyre circulation onto the overturning (e.g., Sidorenko et al., 2021; Sun & Bleck, 2001; Xu et al., 2018). With an appropriate choice of the density coordinate, and with the restriction that it only presents a zonally averaged picture, it allows near-adiabatic large-scale flow along isopycnals to be distinguished from diapycnal flow, and the rate of diabatic density transformation (resulting from a combination of the physical, and, in the case of models, numerical contributions to mixing, and processes associated with the nonlinear equation of state) may be estimated from the divergence of the flowlines (e.g. Lee et al., 2010; Megann, 2018). Sidorenko et al. (2021) analyzed the AMOC in density space in the FESOM ocean model, and in addition used estimates of the diapycnal transports through two-dimensional density surfaces to conclude that dense water formation in the eastern side of the North Atlantic was substantially stronger than in the Labrador Sea,

The surface-forced streamfunction analysis (e.g., Marsh, 2000) is based on the watermass transformation framework of Walin (1982) and of Speer & Tziperman (1992), and relates the rate of density transformation in a given latitude and density class to the surface buoyancy fluxes into that density class over its outcrop area. In a steady state, and in the absence of mixing processes, cabbeling and thermobaricity, the surface-forced streamfunction Ψ_{surf}, at a given latitude and density, would converge to Ψ, the time-averaged overturning streamfunction. In

the real world, Ψ_{surf} evaluated from monthly surface fields as an annual mean has been found to be a good approximation to Ψ, with the caveat that the overturning at a given latitude results from an accumulation of the buoyancy fluxes over a period of between five and ten years, with longer lags generally observed at lower latitudes. This technique has been applied to a range of datasets including reanalyses (Grist et al., 2012; Josey et al., 2009), forced ocean models (Grist et al., 2012; Kostov et al., 2019); coupled climate models (Josey et al., 2009) and hydrographic data (Desbruyères et al., 2019). All of these studies have confirmed that there is a significant level of correlation between the strength of the surface forced streamfunction and that of the overturning streamfunction, with an appropriate lag applied: Josey et al. (2009) used a combination of the HadCM3 coupled model and the NCAR reanalysis, and found that the lag between surface forcing and the overturning increased equatorward from 6 years at 65°N to 15 years at 36°N. Desbruyères et al. (2019) estimated Ψ_{surf} using observational SST and SSS and surface fluxes from the NCEP2, ERA-I, and CERES climatologies, defining annual indices from the maximum values of the respective streamfunction, and again found significant lagged correlations between surface forced streamfunctions and observed estimates of AMOC strength at 45°N. Kostov et al. (2019) investigated the sensitivity of the AMOC strength to variations in the surface fluxes over the seasonal cycle, and found delays of between 8 and 80 months, depending on the season in which the flux anomalies occur.

In this paper we address the questions of in which locations, and by which mechanisms, the variability of the AMOC on timescales from interannual to decadal from the 1970s to the present day is driven. We use a set of three hindcast integrations of a global 1/4° NEMO ocean configuration, with a selection of standard surface forcing datasets, and use the surface-forced streamfunction technique to relate the regional variability of surface fluxes to watermass formation, and thence to the variability of the strength of the meridional overturning. In Section 2 we describe the model configuration and the experimental design, and in Section 3 we introduce the methodology and analysis. In Section 4 we describe the decadal evolution of the AMOC in the simulations, using the surface-forced streamfunction framework to relate this to changes in the surface buoyancy loss. We demonstrate that the decadal-timescale variability is caused mainly by variability in the wintertime heat loss, primarily in the Irminger Sea, and discuss the local causes of heat flux variability, relating the latter to principal North Atlantic climatic indices. In Section 5 we summarize our results and discuss their significance.

2. Model description

The model is the GO6 configuration (Storkey et al. 2018), consisting of version 3.6 of the NEMO ocean model (Madec, 2017), and the GSI8.1 configuration of the Los Alamos National Laboratory sea ice model, CICE (Ridley et al. 2017). The latter consists of version 5.1.2 of the CICE base code with multi-layer, energy-conserving thermodynamics (Bitz & Lipscomb, 1999), elastic-viscous-

plastic ice rheology (Hunke &Dukowicz, 1997) and multi-category ice thickness (Bitz et al., 2001) with 5 thickness categories. Details of the availability of the code are in Appendix A. The grid is the eORCA025 global ¼° grid. Ice shelf cavities are closed, and the freshwater fluxes under the ice shelf are prescribed.

The vertical mixing parameterization scheme is a modified version of the Gaspar et al. (1990) turbulent kinetic energy (TKE) scheme (Madec et al., 2017). The Lagrangian iceberg model of Bigg et al. (1997) and Martin &Adcroft (2010), which was implemented in NEMO by Marsh et al. (2015) is used.

2.2 Initialization and forcing of model integrations

The simulations were all initialized at rest from a climatology based on a mean of years 2004-2008 of the EN3 climatology (Ingleby and Huddleston, 2007. Three datasets (see Table 1) are used to force the ocean integrations: CORE2 (Large et al., 2009), DFS5.2 (Dussin et al., 2016), JRA55-do v1.3 (Tsujino et al., 2018), with the latter updated to JRA55-do v1.5 for the last six years.

The JRA55 integration was forced with a combined precipitation field (as required for NEMO v3.6) that was constructed from the rainfall and snowfall fields from the JRA55 dataset.

3. Analysis methodology

We define the buoyancy flux per unit area F (e.g., Schmitt et al., 1989) as

$$F_\rho = -\varrho \left(\alpha \frac{Q_H}{\varrho C_P} - \beta \frac{\mathrm{S}\ \mathrm{Q_{FW}}}{1-S} \right) \quad (1)$$

where and are the thermal expansion and haline compressibility, respectively; S is the salinity, is a reference density equal to 1026 kg m^{-3}, Q_H is the net downward heat flux per unit area; Q_{FW} is the net freshwater volume flux per unit area into the ocean; and C_p is the specific heat capacity, set here to 3990 J kg^{-1} K^{-1}. F has the dimensions of kg m^{-2} s^{-1}.

We shall use the regions for analysis defined in Table 2 (also illustrated in Figure 2).

The surface-forced streamfunction Ψ_{surf} (,Θ) (Marsh, 2000, and elaborated by Grist et al., 2009) expresses the rate of density transformation by surface buoyancy fluxes at latitude Θ, apportioned into density classes:

$$\Psi_{\mathrm{surf}}(\rho, \Theta) = \frac{(D(\rho,\Theta) - D(\rho+\Delta\rho,\Theta))}{\Delta\rho} \quad (2)$$

where $D(,\Theta)$ is the area integral of the surface buoyancy flux F , as defined in Equation (1), into the surface density range (, +), evaluated from the most northerly surface outcrop of the isopycnal to some fixed northern boundary, and we assume a steady state. Because the rows of the eORCA025 grid are not parallel to lines of constant latitude at high northern latitudes, the integrals were carried out on grid rows, rather than lines of given latitude, and the northern boundary was defined as a constant j-index: this was set to j=1100, corresponding in the North Atlantic domain discussed here to latitudes between

75°N and 78°N. In the results presented here, annual means of $\Psi_{\mathrm{surf}}(\ ,\Theta)$ are evaluated from monthly mean model fields; although this averaging time will miss dense water formation events on shorter timescales, it was the highest frequency available, and errors in general are unlikely to be large (see e.g. Marsh, 2000), although – as we note in Section 4.2 - the rarity of ventilation of the very densest waters may lead to significant inaccuracies for these density classes. If transformation rates due to interior mixing processes and the effects of nonlinearity of the equation of state are relatively small compared with the those of the surface transformations, and if we can neglect changes in isopycnal volume on annual timescales, $\Psi_{\mathrm{surf}}(\ ,\Theta)$ will be a good approximation to the full overturning streamfunction in density classes $\Psi(\ ,\Theta)$, with a lag corresponding to some propagation time at a given latitude Θ, which we shall investigate in Section 4.3. Here we define the density as $\ _2$, the potential density with reference to 2,000 dbar pressure, and this is evaluated in 72 density classes, spanning the range $30.0 < \ _2 < 37.2$ kg m^{-3}: a linear density scale was used for the density classes for $\ _2 < 35.0$ kg m^{-3}, while a logarithmic mapping was used at densities higher than 35.0 kg m^{-3} in order to have an acceptable representation of deep and bottom waters.

The annual overturning streamfunction $\Psi(\ ,\Theta)$, evaluated from monthly mean velocities mapped onto intervals of the monthly mean density, is generally quite smooth in time, allowing the overturning strength to be usefully characterized by a maximum value in a given latitude and depth or density range. By contrast, the annual surface-forced streamfunction has been found (e.g., Desbruyères et al., 2019; Grist et al., 2009) to be rather noisy, both in density and in time, rendering the use of single maxima less helpful. We therefore define indices $\mathrm{T_{OV}}(\mathrm{t})$ and $\mathrm{T_{SF}}(\mathrm{t})$ for the mean overturning and surface-forced streamfunctions, respectively, as functions of time, by evaluating the mean of the respective streamfunction over a region of density and latitude space which reliably contains the maxima of the annual mean streamfunction (allowing for more than one maximum). For the present study, we use the fixed latitude band 48°N-58°N and the density range $36.55 < \ _2 < 36.95$ (corresponding to a depth range between about 900m and 2,000m), which contains the maxima of the streamfunction in almost all years. We find that the overturning streamfunction has reached a near-equilibrium after the first 15 years; since the data used to generate the forcing fields are sparse before the 1970s anyway, we treat this as a spinup period. We subtract the mean value over the period from 1976 until the end of the respective integration to give an anomaly timeseries.

4. Results

4.1 Overturning strength

Figure 1 shows time series of the overturning strength, defined as the maximum of the Atlantic overturning streamfunction in the depth range 900-1100 m, at latitudes 26°N and 45°N, evaluated from the annual mean velocity field, and in the lower two panels the anomalies with respect to the means at each section from 1976 to the end of the respective integration. The AMOC at 26°N from the

RAPID array after 2004 (Smeed et al., 2018) is overlain (cyan lines) onto the AMOC strength for 26°N. It can be seen that the overturning strength in the experiments forced by the CORE2 (black) and DFS5.2 (red) is rather similar at both latitudes, but that in the JRA55-forced experiment (green) is consistently 3-4 Sv weaker. The interannual variability of the AMOC at 45°N is more closely synchronized between the three integrations than it is at 26°N, suggesting that internal, possibly stochastic, processes are more important at the more southerly latitude. The observed AMOC strength at 26°N is intermediate between those in the experiments forced with DFS5.2 and with JRA55.

The CORE2-forced GO6 1/4° configuration described by Storkey et al. (2018) spun up from initialization in 1976 to an unrealistically high AMOC strength at 26°N of over 24 Sv in the 1980s and 1990s, and the CORE2 simulation described here (the black curve in Figure 1(a)) follows a similar trajectory from its start in 1958, albeit with a slower rate of initial strengthening. The reasons for the rise in strength and for the unrealistically strong AMOC over the first decade or two are not yet fully understood. The simulation described here forced with DFS5.2 (red curve in Figure 1(a)) closely follows the CORE2-forced simulation, while the JRA-55 simulation by contrast has a much-reduced spinup transient and, as noted earlier, has a weaker AMOC after this period.

The AMOC anomaly time series (lower panels of Figure 1; note the change in the horizontal axis between the upper and lower panels) shows that the evolution of the AMOC on interannual to decadal time scales in the simulations, after the first 18 years of spinup, is much more consistent between the three integrations once the long-term mean is subtracted. The decadal-timescale evolution over this period is qualitatively consistent with an AMOC index estimated at 50°N from proxy data by Delworth et al. (2016): the latter index rises similarly from the mid-1970s to a maximum in the early 1990s, declining thereafter until about 2010.

Figure 2 shows the mean March mixed-layer depth (defined as the depth at which the density is 0.010 kg m^{-3} higher than that at 10m depth) in the North Atlantic in the three experiments (Figures 2(a-c)), and the maximum values of the surface potential density $_2$ in each year (Figures 2(d-f)), all averaged here over the decade 1996 to 2005, the latter period chosen for consistency with the analysis in Storkey et al. (2018). The boundaries of the four regions used in our analysis are shown as rectangles superposed onto the left-hand panels. In all the simulations, there is winter convection reaching deeper than 500m in all four regions, and the convection depth in the Labrador Sea exceeds 1,000m in all three integrations. The integration forced with CORE2 (Figure 2(a)) can be seen to have much stronger convection in the Nordic Seas than the other two, with patches of mixing exceeding 1,000m, while the JRA55-forced experiment (Figure 2(c)) has shallower convection at all sites, consistent with the weaker overturning seen at both 26°N and 45°N in Figure 1(a) and (b). North of 65°N (which we class here as the Nordic Seas), densities above $_2$=37.1 kg m^{-3} are ventilated; in the Labrador Sea, deep mixing occurs for densities in the range

36.9-37.1 kg m^{-3}; in the Irminger Sea the range is 36.5-36.9 kg m^{-3}; and in the eastern subpolar Atlantic the ventilation is of densities from 36.3 to 36.6 kg m^{-3}. In the Nordic Seas the surface density is substantially higher with CORE2 forcing, reaching a maximum of over 37.5 kg m^{-3} in a patch at around 75°N, while in the other two experiments this density is only attained in the far north-east, just south of Svalbard. All three simulations have strong winter heat loss from the Labrador and Irminger Sea, and also in the far north of the Nordic Seas and in the north-west corner of the North-East Atlantic box. It is interesting that the locations of strongest heat loss are not necessarily coincident with those of deep mixing; in particular, the strong convection in the Greenland Sea in the CORE2 simulation is considerably to the south-west of the near-boundary heat loss, while the dense water formation in the Labrador Sea is in the center of the basin, where the heat loss is around the boundary. This is consistent with the role proposed for eddies by Chanut et al. (2008), Katsman et al. (2018) and others in transporting cold water towards the center of the Labrador Sea to precondition for convection; Megann &Storkey (2021) showed that, although eddies are not usefully resolved at these latitudes in this model configuration, the low default value of the viscosity allows energetic noise-like features in the velocity field that are likely to replace mesoscale eddies in this role.

4.2 Overturning and surface-forced streamfunctions in density space

Figure 3 shows the Atlantic overturning (upper panels) and surface-forced streamfunctions (lower panels) in potential density classes, expressed as functions of $_2$ and averaged over the period 1996-2005. The white areas in the surface-forced streamfunction panels indicate density classes that are not ventilated at those latitudes. The cyan dashed box overlain onto Figure 3(d) encloses the region defined in Section 3 over which we evaluate the indices $T_{OV}(t)$ and $T_{SF}(t)$ for the overturning and surface-forced streamfunctions; the black boxes on the same panel enclose density and latitude ranges typical of deep convection in each of the four regions denoted in Figure 2(a).

The overturning streamfunctions in potential density space (the upper three panels of Figure 3) reveal a clear overall picture: light waters with densities less than $_2$=36.7 enter the basin from the south, and become progressively densified by surface buoyancy losses as they travel north between 45° and 65°N. The resulting dense waters, with $_2$ between 36.80 and 37.05 kg m^{-3}, return southwards as North Atlantic Deep Water (NADW). In this latter southward-flowing leg, the upper part ($_2$<36.9 kg m^{-3}) undergoes a gradual reduction in density resulting from a combination of physical and numerical mixing (see Megann, 2018, for an analysis of the latter in a similar NEMO configuration), while the waters denser than $_2$ > 36.9 kg m^{-3} become yet denser, probably through mixing with the underlying Antarctic Bottom Water (AABW). The overturning cell is weaker in the JRA-55 experiment (Figure 3(c)) than in the other two, with a maximum of 20 Sv, compared with 24 Sv, and lies at lighter densities ($_2$=36.65 kg m^{-3}, compared with 36.70 kg m^{-3} with CORE2 and 36.73 kg m^{-3} with DFS5.2). We note that Arctic waters do not appear to contribute

significantly to the NADW that is exported southwards, since no streamlines from the Arctic continue southward of 68°N: a known weakness of this model configuration is that much of the dense water that enters the subpolar gyre through the Denmark Strait and over the Iceland-Faeroes-Scotland Ridge is rapidly transformed by unphysically large numerical entrainment as it sinks south of the sills.

As discussed by Sidorenko et al. (2021), the overturning streamfunction represents the sum of processes, including surface buoyancy forcing, mixing and also contributions from the non-linear equation of state (cabbeling and thermobaricity). The use of the surface-forced streamfunction (lower panels) allows us to specifically identify the contribution of surface forcing to watermass transformations; the differences between the overturning and surface-forced streamfunctions may be understood as arising from a combination of mixing, cabbeling, thermobaricity and truncation errors due to the use of monthly mean fields. Indeed, we see that the overall form of the overturning circulation is well explained by the surface forcing, with the exception of the continuing densification north of 65°N, contrasting with the overturning streamfunctions which do not display any southward transport for densities greater than $_2$ = 37.1 kg m^{-3}.

As reported by Marsh (2000) and others, there are two lobes in the surface-forced streamfunctions, corresponding to different locations of density transformation. In the simulations described here, Ψ_{surf} has two clear maxima in the CORE2- and DFS5.2-forced cases (Figure 3(d) and (e)), the upper lobe centered at $_2$ 36.40 kg m^{-3}, typical of wintertime surface density in the eastern North Atlantic, associated with the formation of Subpolar Mode Water (SPMW), and the lower one at $_2$ 36.85 kg m^{-3}, closer to winter densities in the Irminger Sea. In the JRA55-forced experiment the lobes are not separated in density space, and the 19 Sv contour encloses both regions: comparison with Figure 2(a)-(c) shows that mixing occurs to about 800m depth south of the Faeroe Islands in CORE2 and DFS5.2, but not in JRA55, which is consistent with the weak upper lobe in Figure 3(f). Further transformation occurs at densities above $_2$ =36.85 kg m^{-3}, which we locate in the Labrador Sea, since this is the only location where such high surface densities are seen in the subpolar gyre, and this is associated with southward transport. So the overall picture is of a chain of densification, first described from observations by McCartney & Talley (1982), which is driven locally by wintertime surface buoyancy losses as water circulates cyclonically around the Subpolar Gyre: first in the north-east, forming SPMW, then in the Irminger Sea, and then finally in the Labrador Sea, resulting in the creation of the model's representation of North Atlantic Deep Water.

In the CORE2 and DFS5.2 experiments the northeast Atlantic and Irminger cells are distinct, suggesting that there is a separate pathway for water of density between $_2$ = 36.35 and 36.5 kg m^{-3} that is created in the former region to be exported southward in these simulations, but the continuity between the Irminger and Labrador regions implies that a pathway exists for water created in the Irminger Sea to enter the Labrador Sea and then be transformed, pos-

sibly by a combination of surface processes and mixing, into the NADW with density higher than $_2 = 36.9$ kg m^{-3} which then propagates southwards. The densest water in the North Atlantic is therefore formed in the Labrador Sea by a combination of local wintertime convection and mixing with water flowing in from the North-East Atlantic region and the Irminger Sea.

We now use the indices T_{OV} and T_{SF}, as defined in section 3, to investigate the time dependence of the surface-forced circulation and to relate this to changes in the overturning strength. In Figures 4(a) and 4(b) we show the time evolution of the two indices for each of the three model integrations. As observed by Grist et al. (2009) and Desbruyères et al. (2019), there is significantly more interannual variability in the surface forced streamfunction T_{SF} than there is in the overturning circulation itself, as represented as T_{OV}; the interpretation is that changes in the latter result (at least partly) from accumulated surface buoyancy fluxes over a few years, which will smooth out such fluctuations. After 1975, all the indices can be seen to increase until the 1990s, after which they decline by about 5 Sv; comparison with Figure 1 confirms that this is consistent with the maximum overturning evaluated in depth space at both 26°N and 45°N. The three experiments again follow one another quite closely, with the JRA55-forced experiment indicating a continuing decline after 2015. To separate the long-term drift due to biases in the forcing datasets, we show the anomalies from the respective means from 1976 to 2005 (Figure 4(c) and (d)): the decadal-timescale evolution of both indices can be seen to be quite consistent between the three integrations, particularly the peak in the overturning strength in 1995 shown in Figure 1 and the subsequent decline (Figure 4(c)). The latter decline is also clearly visible in the surface-forced indices (Figure 4(d)), but the maximum occurs earlier, with two peaks between 1989 and 1995. As already noted, there is considerable interannual variation in the surface-forced indices, with typical amplitude similar to that of the long-term changes, but the interannual variability is quite well correlated between the different forcing datasets.

4.3 Construction of a surface-forced overturning index

Josey et al. (2009) note a maximum correlation between the strength of the overturning and the maximum surface forced streamfunction in a coupled model and the NCAR reanalysis, where the latter time series is lagged by between 6 years and 15 years at 36°N, with the delay increasing towards higher latitudes, while the results of Desbruyères et al. (2019) suggest a shorter delay of between three and six years. Both these observations are consistent with a hypothesis that the overturning circulation is driven predominantly by the accumulated surface buoyancy loss from certain density classes over a handful of preceding years. To verify this for the model integrations described here, we define a synthetic surface forced index T_{int} for a given year. To test the sensitivity to the time scale, we accumulate the surface-forced index T_{SF} in five different ways: as the mean of the surface forced index over the preceding five and ten years, respectively, with constant weights; and as means over five, ten and fifteen years with the weights ramped up linearly from zero to a given year. Table 3 shows the cor-

relation coefficients r between the respective unlagged overturning index T_{OV} and the synthetic surface-forced indices T_{int} for each of the experiments and the ensemble mean, the correlation evaluated over the period between 1976 and the end of the respective time series. The correlation coefficients are consistently highest for the 10-year ramp and the 15-year ramp, with lower coefficients obtained for the shorter time scales for the accumulation. The comparatively high values of r for the JRA experiment are likely to arise from the lower interannual variability in that integration. The fact that the choice of accumulation timescale changes the number of degrees of freedom of the time series, as also does the different length of each of the integrations, makes direct comparison of the correlation coefficients questionable, but examination of Figure 5 supports the conclusion that the ten-year ramp gives qualitatively closer agreement between this surface-forced index and the overturning index. This is consistent with the longer timescales of up to ten years observed by Josey et al. (2009) for the influence of changes in surface buoyancy fluxes on the overturning circulation.

In Figure 5 we show the overturning index for each of the integrations, overlain with the surface forced index lagged by zero, five and ten years (panels (a)-(c)), and the overturning index with the integral index T_{int} accumulated using a 5-year box with constant weights, a ten-year ramp and a fifteen-year ramp (Figures 5(d), (e) and (f), respectively). As noted in the forementioned studies, the lagged surface forced index follows the overturning index over decadal time scales, but it is noisy on interannual frequencies, with steps of up to 4 Sv between successive years; its usefulness as a predictor of overturning changes is therefore limited, regardless of the lag chosen. The integral index, however, tracks the overturning strength much more closely, especially using the ten-year ramp (Figure 5(e)), which not only echoes the decadal changes in overturning strength but also shows some agreement in the interannual variations.

4.4 Geographical distribution of surface buoyancy loss

We now examine the connection between decadal changes in the overturning strength and the components of the buoyancy flux in the regions of dense water formation in the subpolar North Atlantic and the Nordic Seas, as defined in Table 2. In each region, we evaluate the wintertime (DJF) buoyancy loss in kg m^{-3} s^{-1} from annual mean heat and freshwater fluxes according to Equation (1) and integrate over the respective ocean surface area. We find that the variability of the buoyancy contributions from the freshwater flux is negligible, in comparison with that from the surface cooling: the standard deviations of the latter all lie below 0.3 x10^6 kg s^{-1}, where those of the former are all above 3.0 x10^6 kg s^{-1}, so we only show here the contribution from heat loss. We emphasize that we only address here the variability in each contribution: our conclusion that variations in freshwater fluxes do not contribute significantly to the decadal changes in overturning strength certainly does not imply that the time-averaged freshwater fluxes are not important to the overturning circulation. Figure 6 shows the anomalies of the contributions of the heat flux to area-integrated buoyancy loss

anomalies over each of the four basins with respect to the 1976-2005 mean, all with the same vertical scale. It may be noted immediately that the evolution of the heat loss from the Irminger Sea (Figure 4(b)) is strikingly similar to that of the streamfunction indices, as well as to that of the AMOC at both 26°N and 45°N, with a clear increase to 1990, followed by an unambiguous decline from then until at least 2010. The heat loss from the Labrador Sea (Figure 4(a)) has a similar evolution, but the signal is less than half of that of the heat loss from the Irminger Basin. The buoyancy losses in the Nordic Seas and in the north-east Atlantic (Figures 4(c) and (d)) have little interdecadal variability, and so these regions contribute little to the long-term changes seen in the overturning circulation. Again, we only discuss the variability, rather than the time-average of these regional heat fluxes: Figure 3 confirms that there is indeed a strong mean buoyancy loss in the Nordic Seas, even if the variability in time is small.

4.5 Attribution of winter buoyancy loss to physical processes

In Section 4.3 we showed that decadal-timescale variations in the AMOC are highly correlated with variations in the strength of the surface-forced streamfunction, when the latter is accumulated over a timescale of around 10 years, which strongly implies that the surface fluxes are the cause of the changes in the overturning strength. In Section 4.4 we demonstrated that the variability in area-integrated buoyancy losses is dominated by changes in the wintertime heat loss from the Irminger Sea, and to a lesser extent by heat loss in the Labrador Sea.

We now address the question of what the proximal causes are of the changes in heat loss in the Irminger and Labrador Seas. In this section we shall present time series of the regional means of the relevant wintertime near-surface fields from each forcing dataset, along with the respective ensemble mean, to indicate which surface processes are most likely to form the dominant contributions to the variability on the timescales we have discussed in previous sections.

Figure 7 shows anomalies of selected winter mean (DJF) surface fields, averaged over the Irminger Sea box, and defined with respect to the mean from 1976 to 2005. The bold dashed black lines are of the ensemble mean of each variable (in other words, the mean of the time series shown by the black, red and green lines), with a gaussian windowed low-pass filter of width 5 years applied, and the bold dashed blue lines show the anomaly of the winter upward heat flux out of the Irminger Sea, low-pass filtered as above, and normalized to have the same variance as the respective forcing field. We note in passing that the wind speed is defined at 10 m above sea level for all the datasets, while the air temperature and humidity are located at 10m above sea level for CORE2 and JRA-55, and at 2m for DFS5.2; we shall refer to the air temperature as "SAT" for brevity, even though the temperature is defined above the sea surface. All of the quantities except for the shortwave radiation are rather consistent between the three forcing datasets; the magnitude of the scatter in the latter quantity across forcing fields is low (of order 1 W m^{-2}) compared to the standard deviation of the net heat fluxes (over 30 W m^{-2}) and is dominated by interannual

variability.

The heat loss anomaly (dashed blue lines) rises to a maximum in around 1992, then falls towards a minimum just before the end of the JRA-55 integration in 2019. The downwelling shortwave heat flux (Figure 7(a)) shows some of the same decadal variability as the net flux, and is in antiphase with the heat loss, but the magnitude of the variation, as remarked above, is only a few percent of that of the net flux. To definitively eliminate it as an important contribution to the decadal variability of the heat flux, we plot in Figure 7(b) the total heat flux minus the shortwave component: the anomaly of the residual (thick black dashed line) overlies the total heat flux anomaly (thick blue dashed line) almost perfectly, so we infer that the variability of the shortwave is indeed negligible in comparison to that of the sum of the latent, sensible and longwave components. The air temperature (Figure 7(c)) and the humidity (Figure 7(d)) both vary in antiphase with the heat flux except in the period 2005-2015. With the relatively short time series available, it is not straightforward to relate the SST anomaly (Figure 7(e)) causally to the heat flux: evaluation of lagged correlations gives maximum correlations of -0.9 with the SST leading the heat loss by 7 years, and +0.5 with SST lagging heat loss by 14 years. By contrast, the air-sea temperature difference (Figure 7(f)) follows the heat loss closely over the whole analysis period. The wind speed (Figure 7(g)), again has a similar evolution to the heat flux until 2010, after which it increases while the heat loss continues to reduce.

To summarize, variations of the net heat loss from the Irminger Sea on interannual-to-decadal time scales are closely correlated with variations of the air-sea temperature difference over the same region, throughout the analysis period from 1976 to 2020. Correlations between the heat flux and both the air temperature and wind speed are strong until 2005, after which stronger winds are partially compensated by warmer air temperatures. The sensible heat flux in the CORE bulk formulae used in the model (Large &Yeager, 2009) is proportional to the product of the air-sea temperature difference and the wind speed, while the latent heat flux is proportional to product of the SST, the relative humidity (which itself closely follows the SST) and the wind speed, and the upwelling longwave flux is dependent on the SST alone. We conclude that the changes in heat flux are dominated by changes in the air temperature until about 2010, while the SST has a stronger influence after this.

As noted in Section 4.4, the area-integrated buoyancy flux over the Labrador Sea evolves in a similar way to both the AMOC and the buoyancy loss from the Irminger Sea but with about half the magnitude of the latter. Figure 8 shows the same time series as Figure 7, but with means evaluated over the Labrador Sea. Again, the shortwave radiation plays a negligible part in the variability, and the closest time series to that of the net heat flux is that of the air-sea temperature difference, although the SST and SAT follow the heat flux much more closely than in the Irminger Sea. The SST here (Figure 8(e)) is much more strongly anticorrelated with the heat flux than in the Irminger Sea, which

implies that the winter air temperature is more directly controlling the SST there, consistent with its closer proximity to the North American land mass.

4.6 Relationship of the AMOC to the NAO

We note that the decadal evolution of the AMOC in all three simulations, as shown in Figure 1, is similar to that of the observed North Atlantic Oscillation (NAO) index (e.g., Robson et al., 2018). The low-pass filtered index shown in Figure 1(a) of Robson et al. (2018), which is derived from the winter surface pressure difference between Reykjavik and Gibraltar, increases to a positive maximum in the first half of the 1990s, is negative throughout the 2000s, then becomes positive in the mid-2010s. Parker et al. (2018) used the ERA-20C climatology (Poli et al., 2016) and the Met Office operational forecasting system GloSea5 (MacLachlan et al. 2015) to show that the path of the Jet Stream in the northwest Atlantic meanders on decadal timescales in a way that is strongly correlated with the winter NAO index: under typical positive NAO conditions the Jet Stream follows a more direct path across the North Atlantic, allowing cold Arctic air north of it to lie over the subpolar gyre, while under a negative NAO a blocking high pressure system tends to create a large northward meander onto Greenland to up to 80°N, bringing subtropical air over the subpolar gyre.

If the cold air outbreaks over the North Atlantic subpolar gyre typical under positive NAO conditions are associated with high heat loss over this region and if they, as we have shown, lead to a stronger AMOC over the following few years (and, conversely, if warmer air temperature in positive NAO phases leads to a reduced heat loss, followed by a weakening of the AMOC), there should be a strong correspondence between the NAO index and the SAT and heat flux indices presented in Figures 7 and 8. Figure 9(a) and (b) show the ensemble mean anomalies of the winter SAT and of the downward heat flux over the Irminger and Labrador Seas, respectively, normalized to unit variance and with the five-year gaussian low-pass filter applied as in Figures 7 and 8, along with the NAO index presented in Figure 1(a) of Robson et al. (2018), the latter index inverted for clarity. Over the Irminger Sea, the SAT varies with the inverted NAO quite closely, although it does not show the peak one would expect from the strong negative NAO in 2009, while the heat flux also broadly follows the NAO until the mid-2000s, but continues to increase despite the cooling air temperature. Over the Labrador Sea, there is a strong covariance between all of the indices: the SAT and the heat flux reach a minimum in the early 1990s, aligned with the positive peak (here shown as a minimum) of the NAO, followed by an increase up to 2010 and a decline up to about 2015, with an upturn in the last five years.

Robson et al. (2018) show (in their Figure 2(c)) that the winter Jet Stream latitude in the northwest Atlantic is correlated with the NAO index, lying predominantly north of its mean path until the mid-1990s, followed by a period until 2010 in which it lies south of the mean. They also show that the speed of the Jet Stream in the North Atlantic is strongly correlated with the NAO, with higher speeds corresponding to positive NAO phase. We interpret this as confir-

mation that the NAO is the dominant influence on the surface air temperature over the subpolar gyre, hence on the formation of Subpolar Mode Water and ultimately, through continuing buoyancy losses, on the forcing of the AMOC. As mentioned in the previous section, the SAT by itself does not explain the variability of the heat flux from 2000 to 2020, since the latter continues to fall after 2000, as do both the overturning and surface-forced indices shown in Figure 5(e), while the SAT continues to cool (reflected in the upward trend in the red line in Figure 9). We therefore conclude that the changes in air temperature over the Irminger Sea associated with the NAO explain well the variation in the heat flux, and therefore the overturning, until 2000, after which the changes are in heat flux are more faithfully explained by advective SST changes in the North Atlantic Current.

5. Summary and discussion

Three integrations of ¼° global NEMO, forced with CORE2, DFS5.2 and JRA55 datasets, have been completed from 1958 to as close to the present day as the forcing data permit; in particular the simulation forced with JRA-55 extends to the end of 2020. We have identified decadal variation of AMOC strength from 1976 that increases up to 1990, then declines to the present, consistent with observed estimates. The three runs with different forcing datasets have consistent variability on interannual-to-decadal time scales, despite an overturning circulation with the JRA-55 forcing that is about 3 Sv weaker than with the other two forcing datasets.

To relate decadal-timescale variation in watermass formation to surface processes, we have calculated the overturning and surface-forced streamfunctions in potential density space, and have defined a pair of indices representing the maximum value of the respective annually averaged streamfunction in the region in density and latitude space of strongest density transformation. We find that an annual index, which we have defined as the surface-forced index averaged with weights falling linearly to zero over the preceding ten years, matches the overturning index more closely than any simply lagged index, at the same time as smoothing out the considerable interannual variability. This indicates that the decadal variability of the overturning strength is primarily driven by buoyancy losses accumulated over this timescale. The density transformations revealed by both streamfunctions give a picture of successive densification around the subpolar gyre that is consistent for all three integrations: subpolar mode water formed in the north-east Atlantic with $_2$ between 36.3 and 36.6 kg s^{-1} is advected into the Irminger Sea, where surface buoyancy loss increases the density to between 36.5 and 36.9, and this is subsequently transformed in the Labrador Sea to Upper North Atlantic Deep Water with densities between 36.9 and 37.0 kg s^{-1} and then exported southwards, as described by McCartney &Talley (1982). In the simulations there is negligible dense Arctic water present in the NADW, despite substantial cooling and convection in the Nordic Seas south of Svalbard, which is likely to be a result of poor representation of Arctic waters upstream of Denmark Strait and of the Iceland-Faeroes-Scotland ridge system, along with

excessive numerical mixing in the overflows.

Evaluation of winter (DJF) means of area-integrated buoyancy fluxes in four regions of wintertime convection (the Labrador Sea, the Irminger Sea, the north-east Atlantic and the Nordic Seas) shows that the variability seen in the overturning strength is mainly due to variation of the heat loss over the Irminger Sea, with the variability of the buoyancy loss from cooling over the Labrador Sea having half the magnitude, while neither cooling of the north-east Atlantic and Nordic Seas, nor freshwater fluxes in any of the regions, has any significant variability, even though the mean values in these regions may be substantial. We therefore conclude that the variability in the AMOC is largely driven by variability in winter heat loss, mainly over the Irminger Sea, but to a lesser extent over the Labrador Sea. This variability is imprinted on the AMOC as a modulation of the volume of dense water formed in the latter two basins as it moves in an anticyclonic sense around the subpolar gyre.

The time evolution of each of the surface forcing fields was compared to that of the net heat flux over the Irminger Sea, and a strong correlation was found with the air-sea temperature difference, and to a lesser degree with the surface humidity and the wind speed, while the variability of the solar shortwave radiation was found to be very low by comparison. This implies that on decadal time scales the air temperature was the main driver of changes in buoyancy losses over the Irminger Sea, and subsequent changes in the AMOC until around the year 2000, when the AMOC changes caused subpolar SST changes, triggering a positive feedback which maintains the AMOC decline. The sensitivity to air temperature, along with the fact that the AMOC anomaly follows that of the North Atlantic Oscillation index, suggests that the two most likely mechanisms for AMOC variability are meandering of the Jet Stream that brings alternately warm and cold air over the subpolar Irminger Sea; and variation of the speed of the Jet Stream that is associated with changes in advection of cold continental air masses over the subpolar North Atlantic, both processes strongly correlated with the NAO.

The use of the density transformation framework, and more specifically the surface-forced streamfunction, provides strong insights into the relationship between changes in surface buoyancy fluxes and changes in watermass properties that are not directly provided by analysis of the overturning in depth coordinates, nor by calculation of winter mixed-layer depths alone. It sidesteps questions regarding the representation of convection in numerical models (they generally use an enhanced diffusivity to mix to a prescribed depth, which is a distinct physical process from convection), and also disregards the issue of preconditioning for convection by salty anomalies in the upper ocean (e.g., Menary et al., 2012; Ortega et al., 2021). As we have demonstrated, the surface-forced streamfunction can in addition be used to derive a scalar index that has predictive skill for the overturning strength. Nevertheless, the density transformation analysis we have presented has its limitations. The streamfunctions are constructed as zonal integrals, so lose information on the longitudinal location of

the buoyancy losses, and also depend on a sufficiently long integration to remove enough noise from the signal for it to be interesting, at the same time as needing possibly impractically short averaging times (almost certainly shorter than the monthly means used here) to faithfully capture extreme buoyancy loss events such as those caused by the Greenland tip jets described by Josey et al. (2019). Extension of this framework to derive transformation rates as a two-dimensional field on given density surfaces, as derived from observational data by Desbruyères et al. (2019) and from numerical models by Xu et al. (2018) and Sidorenko et al. (2021) can provide much more detailed information on the processes of density transformation, but we have not evaluated these fluxes here.

There have been recent suggestions that the AMOC is currently in a recovery phase after the decline reported by Smeed et al. (2018) and others. The overturning and surface-forced indices derived by Desbruyères et al. (2019) from observational datasets show a decline of about 3 Sv from 1993 to 2010, followed by a sharp increase of about 4 Sv between 2010 and 2018. Moat et al., (2020) used data from the RAPID array at 26°N to estimate a recovery of a similar magnitude over the same period. This is not seen robustly in our simulations: the AMOC strength at both 26°N and 45°N in the JRA-55 forced experiment (the green lines in Figure 1) shows a continuing decline of about 2 Sv from 2010 to 2020, possibly levelling out in the final years. The overturning indices we have derived from the surface buoyancy fluxes (Figure 5(e)) are equivocal: while those for JRA-55 are consistent with the continuing weakening in the AMOC in that experiment, those for the DFS5.2-forced simulation suggest an upturn after 2010, although the latter dataset ends in 2015, so robust conclusions may not be reached. Applying the analysis presented here to integrations forced by a different forcing dataset, such as ERA-5 (Hersbach et al., 2020), is likely to strengthen any predictions, and work by the authors to investigate this is underway using an ensemble based on a more recent ¼° NEMO configuration. Nevertheless, we have clearly demonstrated the potential of this technique as a predictive tool as predictive tool for the AMOC strength, and the availability of surface field datasets that are continuously updated to a few months behind the present.

Acknowledgments

The work was supported by funding from the Natural Environment Research Council (NERC) under the Atlantic Climate System Integrated Study (ACSIS) project (NE/N018044/1), with additional funding from European Union's Horizon 2020 research
and innovation programme COMFORT (grant agreement No. 820989) and additional support by the NERC WISHBONE project (reference NE/T013540/1). The model integrations were completed on the Archer supercomputing system and on the NEXCS platform at the UK Met Office, both facilities funded by NERC and the Engineering and Physical Science Research Council (EPSRC). Analysis was carried out on the JASMIN platform, funded by NERC. We are

grateful for invaluable assistance from Computational Modelling Services at the National Centre for Atmospheric Science. We would also like to thank Ed Blockley, Jeremy Grist, Ben Moat, Jon Robson and Dave Storkey for advice and assistance, and Richenda Houseago-Stokes and Helen Snaith for archiving the model output to BODC.

Appendix A: Code documentation

The ocean model code is available from the NEMO website (www.nemo-ocean.eu) under the CeCILL free software license (http://www.cecill.info/). On registering, individuals can access the Fortran code using the open-source subversion software (http://subversion.apache.org/). The base code used for the integrations presented in this paper is in revision 7750 of the

following branch: http://forge.ipsl.jussieu.fr/nemo/svn/NEMO/branches/UKMO/dev_r5518_GO6_package.

This consists of the NEMO v3.6 release with the addition of GO6-specific changes. The sea ice model code is freely available from the Met Office Science Repository (https://code.metoffice.gov.uk/trac/cice) under the CICE copyright agreement (http://oceans11.lanl.gov/trac/CICE/wiki/CopyRight) and the Fortran code is available using subversion. The code used for the integrations presented in this paper consisted of a number of branches of the CICE code. These branches have subsequently been merged into a single package branch (vn5.1.2_GSI8.0_package_branch) at revision 235.

The following preprocessing keys were applied in building GO6-GSI8.1: key_trabbl; key_si3; key_zdftke; key_zdfddm; key_mpp_mpi; key_mpp_rep; key_nosignedzero; key_iomput

Appendix B: Data access and availability

The output from the integrations described here is archived by the British Oceanographic Data Centre (BODC) at the Centre for Environmental Data Analysis (CEDA). It is available as follows:

CORE2 (suite identifier u-ap795): https://data.ceda.ac.uk/bodc/SOC210128

DFS5.2 (suite identifier u-ao882): https://data.ceda.ac.uk/bodc/SOC210129

JRA-55 (suite identifier u-ba494): https://data.ceda.ac.uk/bodc/SOC210130

References

Bigg, G. R.,Wadley, M. R., Stevens, D. P., and Johnson, J. A.: Modelling dynamics and thermodynamics of icebergs, *Cold Reg. Sci. Technol.,* **26**, 113–135, 1997.

Bitz, C. M., Holland, M. M., Weaver, A. J., and Eby, M.: Simulating the ice-thickness distribution in a coupled climate model, *J. Geophys. Res.-Oceans*, **106**,

Bitz, C. M. and Lipscomb, W. H.: An energy-conserving thermodynamic model of sea ice, J. *Geophys. Res.-Oceans,* **104**, 15669–15677,

https://doi.org/10.1029/1999JC900100, 1999.

Bleck, R. & Sun, S. (2004). Diagnostics of the oceanic thermohaline circulation in a coupled climate model. *Global and Planetary Change* **40**: 233-248.

Chafik, L., & Rossby, T., (2019). Volume, heat, and freshwater divergences in the subpolar North Atlantic suggest the Nordic Seas as key to the state of the meridional overturning circulation. *Geophys Res Lett*, 46, 4799–4808. https://doi.org/10.1029/2019GL082110

Chanut, J., B. Barnier, W. Large, L. Debreu, T. Penduff, J-M Molines & P. Mathiot, (2008). Mesoscale Eddies in the Labrador Sea and Their Contribution to Convection and Restratification. *J. Phys. Oceanog.* **38**, 1617-1647.

Cheng, W., Chiang, J.C.H., & Zhang, D. (2013). Atlantic meridional overturning circulation (AMOC) in CMIP5 models: RCP and historical simulations. *J. Climate*, **26**, 7187–7197, https://doi.org/10.1175/JCLI-D-12-00496.1.

Curry, R. G., McCartney, M. S., & Joyce, T. M. (1998). Oceanic transport of subpolar climate signals to mid-depth subtropical waters. Nature, 391, 575–577, doi:10.1038/35356.

Danabasoglu, G., Yeager, S.G., Kwon, Y-O., Tribbia, J.J., Phillips, A.S., & Hurrell, J.W. (2012). Variability of the Atlantic Meridional Overturning Circulation in CCSM4, *Journal of Climate* 25, 15 (2012): 5153-5172 https://doi.org/10.1175/JCLI-D-11-00463.1

Delworth, T., Zeng, F., Vecchi, G. *et al.* (2016). The North Atlantic Oscillation as a driver of rapid climate change in the Northern Hemisphere. *Nature Geosci* **9,** 509–512, doi:10.1038/ngeo2738

Desbruyères, D.G., Maze, G., & Daniault, M. (2019). Surface predictor of overturning circulation and heat content change in the subpolar North Atlantic. *Ocean Sci.*, **15**, 809–817. https://doi.org/10.5194/os-15-809-2019

Desbruyères, D., Chafik, L., & Maze, G. (2021). A shift in the ocean circulation has warmed the subpolar North Atlantic Ocean since 2016. *Nature Comms Earth and Environment* **2**:48 https://doi.org/10.1038/s43247-021-00120-y

Dong, B. & Sutton, R.T. (2005). Mechanism of Interdecadal Thermohaline Circulation Variability in a Coupled Ocean–Atmosphere GCM, *J. Climate*, **18**(8), 1117–113, https://doi.org/10.1175/JCLI3328.1

Dussin, R., Barnier, B. & Brodeau, L. (2016). The making of Drakkar forcing set DFS5. DRAKKAR/MyOcean Report 01-04-16, LGGE, Grenoble, France.

Eden, C., & Willebrand, J. (2001). Mechanism of Interannual to Decadal Variability of the North Atlantic Circulation. *J. Climate* **14**, 2266-2280.

Gaspar, P., Grégoris, Y., & Lefevre, J.-M. (1990). A simple eddy kinetic energy model for simulations of the oceanic vertical mixing: tests at Station Papa

and long-term upper ocean study site, *J. Geophys. Res.,* **95**, 16179–16193, doi:10.1029/JC095iC09p16179.

Good, S. A., Martin, M.J., & Rayner, N.A. (2013). EN4: quality-controlled ocean temperature and salinity profiles and monthly objective analyses with uncertainty estimates, *JGR: Oceans*, **118**, 6704-6716.

Grist, J.P., Marsh, R.A., & Josey, S.A. (2009). On the Relationship between the North Atlantic Meridional Overturning Circulation and the Surface-Forced Overturning Streamfunction. *J. Climate* **22**, 4989-5002

Grist, J. P., Josey, S.A., & Marsh, R. (2012). Surface estimates of the Atlantic overturning in density space in an eddy-permitting ocean model. *J. Geophys. Res.* **117**, C06012. doi:10.1029/2011JC007752

Grist, J.P., Josey, S.A., & Marsh, R. Kwon, Y.-O., Bingham, R.J., & Blaker, A.T. (2014). The Surface-Forced Overturning of the North Atlantic: Estimates from Modern Era Atmospheric Reanalysis Datasets. *J. Clim.* **27**, 3596-3618 (2014). doi:10.1175/JCLI-D-13-00070.1

Hersbach, H. et al., (2020). The ERA5 Global Reanalysis. QJRMS https://doi.org/10.1002/qj.3803.

Hunke, E.C., & Lipscomb, W.H., (2010). CICE: The Los Alamos Sea Ice Model, Documentation and Software User's Manual, Version 4.1. Tech. Rep. LA-CC- 06-012, Los Alamos National Laboratory, Los Alamos, New Mexico. http://oceans11.lanl.gov/trac/CICE.

Ingleby, B. & Huddleston, M. (2007). Quality control of ocean temperature and salinity profiles – historical and real-time data, *J. Marine Syst.,* **65**, 158–175.

Josey, S. A., Grist, J.P., & Marsh, R. (2009). Estimates of meridional overturning circulation variability in the North Atlantic from surface density flux fields, *J. Geophys. Res.,* **114**, C09022, doi:10.1029/2008JC005230.

Josey, S. A., de Jong, M. F., Oltmanns, M., Moore, G. K., & Weller, R. A. (2019). Extreme variability in Irminger Sea winter heat loss revealed by ocean observatories initiative mooring and the ERA5 reanalysis. *Geophys. Res. Lett.* **46**, 293–302. https://doi.org/10.1029/2018GL080956

Katsman, C. A., Drijfhout, S. S., Dijkstra, H. A., & Spall, M. A. (2018). Sinking of dense North Atlantic waters in a global ocean model: Location and controls. *Journal of Geophysical Research: Oceans,* **123**, 3563–3576. https://doi.org/10.1029/2017JC013329

Kieke, D., & Yashayaev, I. (2015). Studies of Labrador Sea Water formation and variability in the subpolar North Atlantic in the light of international partnership and collaboration. Prog. Oceanogr., 132, 220–232, doi:10.1016/j.pocean.2014.12.010.

Kostov, Y. Johnson, H.L. & Marshall, D.P. (2019). AMOC sensitivity to surface buoyancy fluxes: the role of air-sea feedback mechanisms. *Climate Dynamics*

https://doi.org/10.1007/s00382-019-04802-4

Kuhlbrodt, T., Griesel, A., Montoya, M., Levermann, A., Hofmann, M., & Rahmstorf, S. (2007). On the driving processes of the Atlantic meridional overturning circulation, *Rev. Geophys.*, doi:10.1029/2004RG0001662007.

Large, W. G. & Yeager, S. G., (2009). The global climatology of an interannually varying air-sea flux data set, *Clim. Dynam.,* **33**, 341–364, doi:10.1007/s00382-008-0441-3, 2009.

Lee, M.-M., Coward, A.C., Nurser, A.G., 2002. Spurious diapycnal mixing of deep waters in an eddy-permitting global ocean model. *J. Phys. Oceanog.* **32**, 1522–1535.

Liu, W., A.V. Fedorov, S-P. Xie & S Hu, (2020). Climate impacts of a weakened Atlantic Meridional Overturning Circulation in a warming climate. *Science Advances* 6. doi: 10.1126/sciadv.aaz4876

Lozier, M. S, Li, F., Bacon, S., Bahr, F., Bower, A. S., Cunningham, S. A., de Jong, M. F., de Steur, L., deYoung, B., Fischer, J., Gary, S. F., Greenan, B. J. W., Holliday, N. P., Houk, Houpert, A., L., Inall, M.E., Johns, W.E., Johnson, H.L., Johnson, C. , Karstensen, J. , Koman, G. , LeBras, I.A. , Lin, X., Mackay, N. , Marshall, D.P. , Mercier, H. , Oltmanns, M. , Pickart, R.S. , Ramsey, A.L. , Rayner, D., Straneo, F. Thierry, V. , Torres, D.J. , Williams, R.G. , Wilson, C. , Yang, J. , Yashayaev, I. , & Zhao, J. (2019). A Sea Change in Our View of Overturning in the Subpolar North Atlantic. *Science*, doi: 10.1126/science.aau6592

MacLachlan, C., Arribas, A., Peterson, K. A., Maidens, A., Fereday, D., Scaife, A. A., et al. (2015). Global Seasonal forecast system version5 (GloSea5): A high resolution seasonal forecast system. *Quarterly Journal of the Royal Meteorological Society*, **141**, 1072–1084. https://doi.org/10.1002/qj.2396

Madec, G. and the NEMO team, (2017). NEMO ocean engine: version 3.6 stable. Note du Pôle de modélisation, Institut Pierre-Simon Laplace (IPSL),

France, No 27 ISSN No 1288–1619. https://doi.org/10.5281/zenodo.3248739. Last accessed: July 2020.

Marsh, R., (2000). Recent variability of the North Atlantic thermohaline circulation inferred from surface heat and freshwater fluxes. *J. Climate*, **13**.

Marsh, R., Ivchenko, V. O., Skliris, N., Alderson, S., Bigg, G. R., Madec, G. et al., Blaker, A. T., Aksenov, Y., Sinha, B., Coward, A. C., Le Sommer, J., Merino, I., and Zalesny, V. (2015). NEMO–ICB (v1.0): interactive icebergs in the NEMO ocean model globally configured at eddy-permitting resolution, *Geoscientific Model Development*, **8**, 1547–1562, doi:10.5194/gmd-8-1547-2015, https://hal-insu. archives-ouvertes.fr/insu-01205192.

Martin, T. and Adcroft, A.: Parameterizing the fresh-water flux from land ice to ocean with interactive icebergs in a coupled climate model, *Ocean Modelling.,* **34**, 111–124, https://doi.org/10.1016/j.ocemod.2010.05.001, 2010.

Mauritzen, C. (1996). Production of dense overflow waters feeding the North Atlantic across the Greenland-Scotland Ridge. Part 1: Evidence for a revised circulation scheme. *Deep-Sea Research Part I: Oceanographic Research Papers,* **43**, 769–806. https://doi.org/10.1016/0967-0637(96)00037-4

McCartney, M. S. & Talley, L.D. (1982). The subpolar mode water of the North Atlantic Ocean *J. Phys. Oceanogr.* **12** 1169-88.

MacLachlan, C., Arribas, A., Peterson, K.A., Maidens, A. , Fereday, D., Scaife, A.A. , Gordon, M., Vellinga, M., Williams, A., Comer, R. E., Camp J., and Xavier, P. 2015. Description of GloSea5: the Met Office high resolution seasonal forecast system. *Q. J. R. Met. Soc.,* DOI: 10.1002/qj.2396.

Megann, A., (2018). Estimating the numerical diapycnal mixing in an eddy-permitting ocean model. Ocean Modelling, **121**. 19-33. DOI: 10.1016/j.ocemod.2017.11.001

Megann, A. & Storkey, D. (2021). Exploring viscosity space in an eddy-permitting global ocean model: is viscosity a useful control for numerical mixing? JAMES, **13**, e2020MS002263. https://doi.org/10.1029/2020MS002263

Menary, M. B., Park, W., Lohmann, K., Vellinga, M., Palmer, M. D., Latif, M. & Jungclaus, J. H. (2012). A multimodel comparison of centennial Atlantic meridional overturning circulation variability. *Climate Dynamics*, DOI 10.1007/s00382-011-1172-4

Menary, M. B., Jackson, L. C. & Lozier, M. S. (2020). Reconciling the relationship between the AMOC and Labrador Sea in OSNAP observations and climate models. *Geophys. Res. Lett.* **47**, e2020GL089793.

Menary, M. B., Robson, J., Allan, R., Booth, B. B. B., Cassou, C., Gastineau, G., Gregory, J., Hodson, D., Jones, C., Mignot, J., Ringer, M., Sutton, R., Wilcox, L. & Zhang, R. (2020). Aerosol-forced AMOC changes in CMIP6

historical simulations. *Geophys. Res. Lett.* e2020GL088166. ISSN 0094-8276 doi: https://doi.org/10.1029/2020GL088166

Moat, B.I., Smeed, D. a., Frajka-Williams, E., Desbruyères, D. G., Beaulieu, C., Johns, W. E., Rayner, D., Sanchez-Franks, A., Baringer, M.O., Volkov, D., & Bryden, H.L. (2020). Pending recovery in the strength of the meridional overturning circulation at 26°N *Ocean Science,* **16** (4). 863-874. https://doi.org/10.5194/os-2019-134

Oltmanns, M., Karstensen, J., & Fischer, J. (2018). Increased risk of a shutdown of ocean convection posed by warm North Atlantic summers**.** *Nature Climate Change*, DOI: 10.1038/s41558-018-0105-1

Ortega, P., Robson, J., Sutton, R.T., & Andrews, M. B (2017) Mechanisms of decadal variability in the Labrador Sea and the wider North Atlantic in a high-resolution climate model *Climate Dynamics* **49** (7), 2625-2647

Ortega, P., Robson, J. I., Menary, M., Sutton, R. T., Blaker, A., Germe, A., Hirschi, J. J.-M., Sinha, B., Hermanson, L. & Yeager, S. (2021). Labrador Sea subsurface density as a precursor of multidecadal variability in the North Atlantic: a multi-model study. *Earth System Dynamics,* **12** (2). pp. 419-438. ISSN 2190-4987 doi: https://doi.org/10.5194/esd-12-419-2021

Otterå, O., Bentsen, M., Drange, H. *et al.* (2010). External forcing as a metronome for Atlantic multidecadal variability. *Nature Geosci* **3,** 688–694, https://doi.org/10.1038/ngeo955

Parker, T., Woollings, T. Weisheimer, A., O'Reilly, C. H., Baker, L., & Shaffrey, L. (2019). Seasonal predictability of the winter North Atlantic Oscillation from a jet stream perspective. *Geophys. Res. Lett,* **46**, 10,159–10,167. https://doi.org/10.1029/2019GL084402

Peings Y & Magnusdottir, G. (2014). Forcing of the wintertime atmospheric circulation by the multidecadal fluctuations of the North Atlantic Ocean, *Environmental Research Letters* **9**(3) 034018 doi:10.1088/1748-9326/9/3/034018

Petit, T., Lozier, M. S., Josey, S. A., & Cunningham, S. A. (2020). Atlantic deep water formation occurs primarily in the Iceland Basin and Irminger Sea by local buoyancy forcing. *Geophysical Research Letters*, **47**, e2020GL091028. https://doi.org/10.1029/2020GL091028.

Pickart, R. S., F. Straneo, & G. W. K. Moore (2003). Is Labrador Sea Water formed in the Irminger Basin? *Deep-Sea Res. I*, **50**, 23–52.

Poli, P.H., Hersbach, H., Dee, D.P., Berrisford, P., Simmons, A.J., Vitart, F., Laloyaux, P., Tan, D.G.H., Peubey, C., Thépaut, J-N., Trémolet, Y., Hólm, E.V., Bonavita, M., Isaksen, L., & Fisher M. (2016). ERA-20C: An atmospheric reanalysis of the twentieth century. *Journal of Climate* **29**(11), 4083-4097. https://doi.org/10.1175/JCLI-D-15-0556.1

Rayner, N. A., Parker, D. E., Horton, E. B., Folland, C. K., Alexander, L. V.,

Rowell, D. P., Kent, E. C., & Kaplan, A. (2003). Global analyses of sea surface temperature, sea ice, and night marine air temperature since the late nineteenth century J. Geophys. Res.Vol. 108, No. D14, 4407 10.1029/2002JD002670

Ridley, J. K., Blockley, E. W., Keen, A. B., Rae, J. G. L., West, A. E., and Schroeder, D.: The sea ice model component of HadGEM3-GC3.1, *Geosci. Model Dev.,* **11**, 713–723, https://doi.org/10.5194/gmd-11-713-2018, 2018.

Roberts, C. D., et al. (2013). Atmosphere drives recent interannual variability of the Atlantic

meridional overturning circulation at 26.5°N, *Geophys. Res. Lett.,* **40**, 5164–5170, doi:10.1002/grl.50930.

Robson, J., Ortega, P. & Sutton, R. (2016). A reversal of climatic trends in the North Atlantic since 2005. *Nature Geosci* **9,** 513–517, https://doi.org/10.1038/ngeo2727

Robson, J., Sutton, R. T., Archibald, A., Cooper, F., Christensen, M., Gray, L. J., Holliday, N. P., Macintosh, C., McMillan, M., Moat, B., Russo, M., Tilling, R., Carslaw, K., Desbruyères, D., Embury, O., Feltham, D. L., Grosvenor, D. P., Josey, S., King, B., Lewis, A., McCarthy, G. D., Merchant, C., New, A. L., O'Reilly, C. H., Osprey, S. M., Read, K., Scaife, A., Shepherd, A., Sinha, B., Smeed, D., Smith, D., Ridout, A., Woollings, T. & Yang, M. (2018). Recent multivariate changes in the North Atlantic climate system, with a focus on 2005-2016. *International Journal of Climatology*, 38 (12). pp. 5050-5076. ISSN 0899-8418 doi: https://doi.org/10.1002/joc.5815

Robson, J., Aksenov, Y., Bracegirdle, T. J., Dimdore-Miles, O., Griffiths, P. T., Grosvenor, D. P., et al. (2020). The evaluation of the North Atlantic climate system in UKESM1 historical simulations for CMIP6. *JAMES*, **12**, https://doi.org/10.1029/2020MS002126

Schmitt, R.W., Bogden P.S., & Dorman, C.E. (1989). Evaporation minus precipitation and density fluxes for the North Atlantic. *J. Phys. Ocean* **19**, 1208-1221.

Schmitz, W. J., & McCartney, M. S. (1993). On the North Atlantic circulation. *Reviews of Geophysics,* **31**, 29–49. https://doi.org/10.1029/92RG02583

Sidorenko, D., Danilov, S., Fofonova, V., Cabos, W., Koldunov, N., Scholz, P., Sein, D., & Wang, Q. (2020). AMOC, water mass transformations and their responses to changing resolution in the Finite-volumE Sea ice–Ocean Model. *Journal of Advances in Modeling Earth Systems***, 12.** https://doi.org/10.1029/2020MS002317

Smeed, D. A., Josey, S. A., Beaulieu, C., Johns, W. E., Moat, B. I., Frajka-Williams, E., et al. (2018). The North Atlantic Ocean is in a state of reduced overturning. *Geophys. Res. Lett.,* **45**, 1527–1533. https://doi.org/10.1002/2017GL076350

Smith, D.M., Scaife, A.A., Eade, R. *et al.* (2020). North Atlantic climate far more predictable than models imply. *Nature* **583,** 796–800, https://doi.org/10.1038/s41586-020-2525-0

Speer, K., & Tziperman, E. (1992). Rates of water mass formation in the North Atlantic Ocean. *Journal of Physical Oceanography*, 22, 93–104. **doi** 10.1175/1520-0485(1992)022

Storkey, D., Blaker, A.T., Mathiot, P. Megann, A., Aksenov, Y., Blockley, E.W., Calvert, D., Graham, T., Hewitt, H.T., Hyder, P., Kuhlbrodt, T., Rae, J.G.L., & Sinha, B. (2018). UK Global Ocean GO6 and GO7: a traceable hierarchy of model resolutions. *Geosci. Model Dev.* **11**, 3187–3213. doi:10.5194/gmd-11-3187-2018.

Stramma, L., Kieke, D., Rhein, M., Schott, F., Yashayaev, I., & Koltermann, K. P. (2004). Deep water changes at the western boundary of the subpolar North Atlantic during 1996 to 2001. Deep-Sea Res. I, 51, 1033–1056, doi:10.1016/j.dsr.2004.04.001.

Sun, S., & Bleck, R. (2001). Atlantic Thermohaline Circulation and its Response to Increasing CO2 in a Coupled Atmosphere–Ocean Model. *Geophys. Res. Lett.* **28**, 4223-4226.

Sutton, R.A., McCarthy, G. D., Robson, J., Sinha, B., Archibald, A. T., & Gray L. J. (2018). Atlantic Multidecadal Variability and the U.K. ACSIS Program, *Bulletin of the American Meteorological Society*, **99** (2), 415-425, https://doi.org/10.1175/BAMS-D-16-0266.1

Tsujino, H., Urakawa, S., Nakano, H., Small, R.J., Kim, W.M., Yeager, S.G., Danabasoglu, G., Suzuki, T., Bamber, J. L., Bentsen, M., Boning, C., Bozec, A., Chassignet, E., Curchitser, E., Boeira Diasi, F., Durack, P.J., Griffies, S.M., Harada, Y., Ilicak, M., Josey, S.A., Kobayashi, C., Kobayashi, S., Komuro, Y., Large, W.G., Le Sommer, J., Marsland, S.J., Masina, S., Scheinert, M., Tomita, H., Valdivieso, M. & Yamazaki, D. (2018). JRA-55 based surface dataset for driving ocean-sea ice models (JRA55-do) *Ocean Modelling,* 130, 79-139 doi: 10.1016/j.ocemod.2018.07.002

Walin, G., (1982). On the relation between sea-surface heat flow and thermal circulation in the ocean. *Tellus* **34**, 187-195.

Worthington, E.L., Moat, B.I., Smeed, D.A., Mecking, J.V., Marsh, R., & McCarthy, G.D. (2020). A 30-year reconstruction of the Atlantic meridional overturning circulation shows no decline. *Ocean Science* **71**. https://doi.org/10.5194/os-2020-71

Worthington, L. V. (1976). On the North Atlantic circulation. *The Johns Hopkins Oceanographic Studies,* **6,** 110.

Xu, X., Rhines, P. B., & Chassignet, E. P. (2018). On mapping the diapycnal water mass transformation of the upper North Atlantic Ocean. *J. Phys. Oceanog.,* **48**, 2233–2258. https://doi.org/10.1175/JPO!D!17!0223.1

Zou S & Lozier, M.S. (2016). Breaking the linkage between Labrador Sea Water production and its export to the subtropical gyre. *Journal of Physical Oceanography.* **46**, 2169-2182.

Zou, S., Lozier, M. S. & Xu, X. (2020). Latitudinal structure of the Meridional Overturning circulation variability on interannual to decadal time scales in the North Atlantic Ocean. *J. Clim.* **33**, 3845–3862.

Forcing set	**Integration**	**Wind speed**	**Radiation**	**SAT, humidity**	**Precipitation**
CORE2	1958-2007	6-hourly	Daily	6-hourly	Monthly
DFS5.2	1958-2015	3-hourly	Daily	3-hourly	Daily
JRA-55	1958-2020	3-hourly	3-hourly	3-hourly	3-hourly

Table 1: Integration period and forcing frequencies used for model integrations

Basin	**Zonal limits**	**Meridional limits**
Labrador Sea	47°N to 65°N	70°W to 40°W
Irminger Basin	47°N to 65°N	40°W to 20°W
North-east Atlantic	47°N to 65°N	20°W to 0°W
Nordic Seas	65°N to 85°N	20°W to 20°E

Table 2 Regions for integration of surface fluxes

Forcing	**CORE2**	**DFS5.2**	**JRA-55**	**Ensemble mean**
Zero lag	0.537	0.660	0.858	0.786
5-year box	0.766	0.912	0.953	0.935
10-year box	0.819	0.898	0.956	0.954
5-year ramp	0.743	0.900	0.955	0.927
10-year ramp	0.859	0.940	0.970	0.968
15-year ramp	0.863	0.929	0.966	0.965

Table 3: Correlations between surface-forced index and the lagged accumulated indices for each of the experiments and for the ensemble mean.

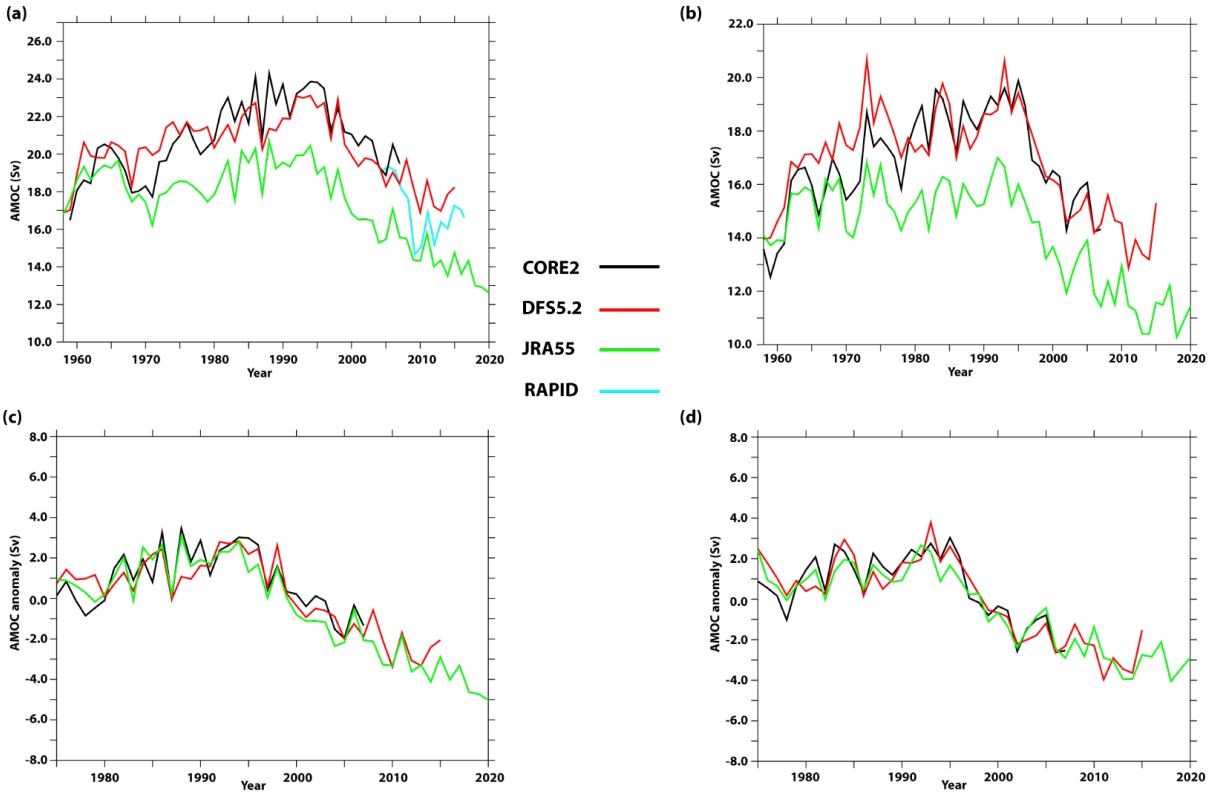

Figure 1. Annual mean AMOC strength at (a) 26°N and at (b) 45°N over the complete model integrations, and the anomaly from the mean (evaluated from 1976 until the end of each integration) at (c) 26°N and at (d) 45°N. The cyan curve in panel (a) is the annual mean (January-December) transport estimated from the RAPID array (Smeed et al., 2018).

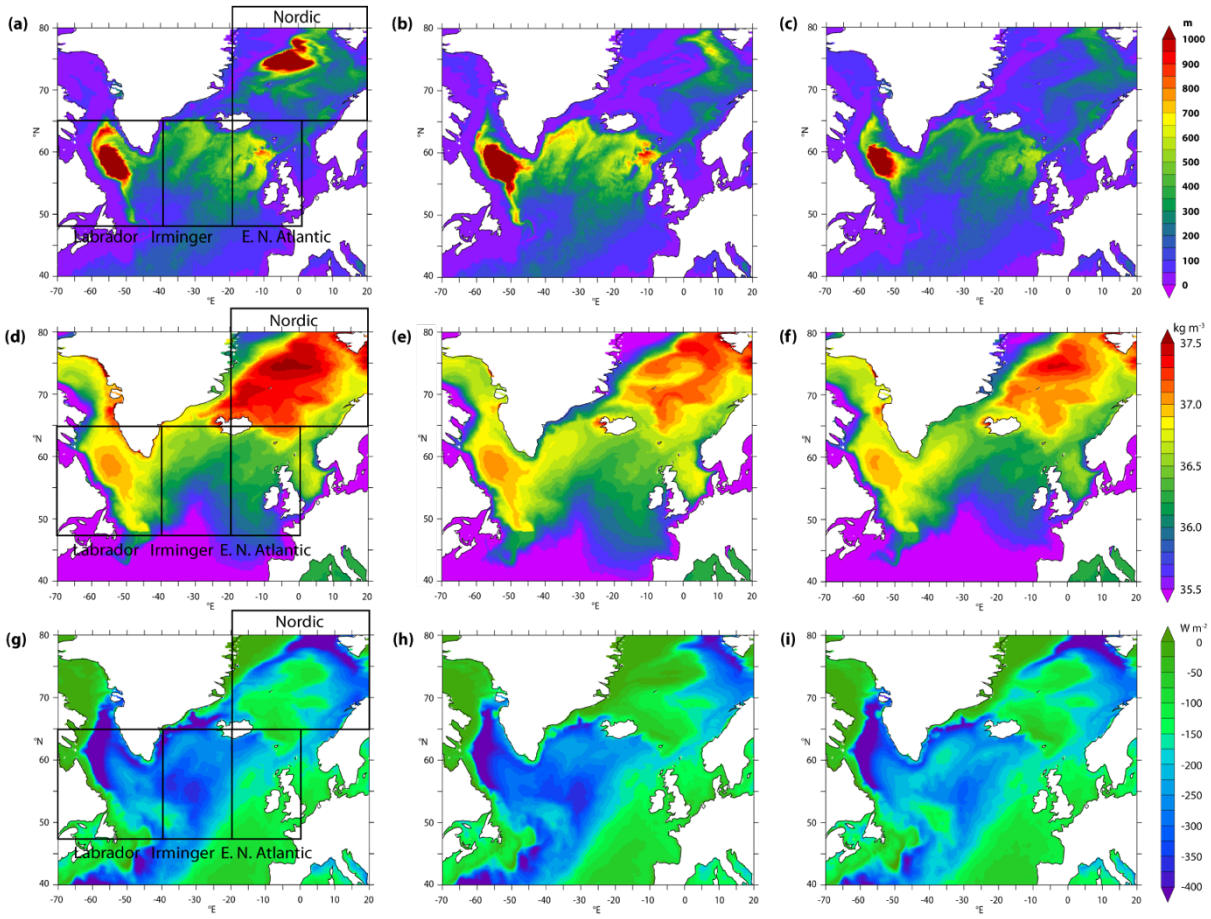

Figure 2. Mean March mixed-layer depth (in m) with (a) CORE2; (b) with DFS5.2; and (c) with JRA-55; and maximum surface potential density $_2$ (in kg m^{-3}) with (d) CORE2; (e) with DFS5.2; and (f) with JRA-55; and mean winter downward heat flux in W m^{-2} with (g) CORE2; (h) with DFS5.2; and (i) with JRA-55. The boxes in the left-hand panels show the regions for analysis defined in Table 2.

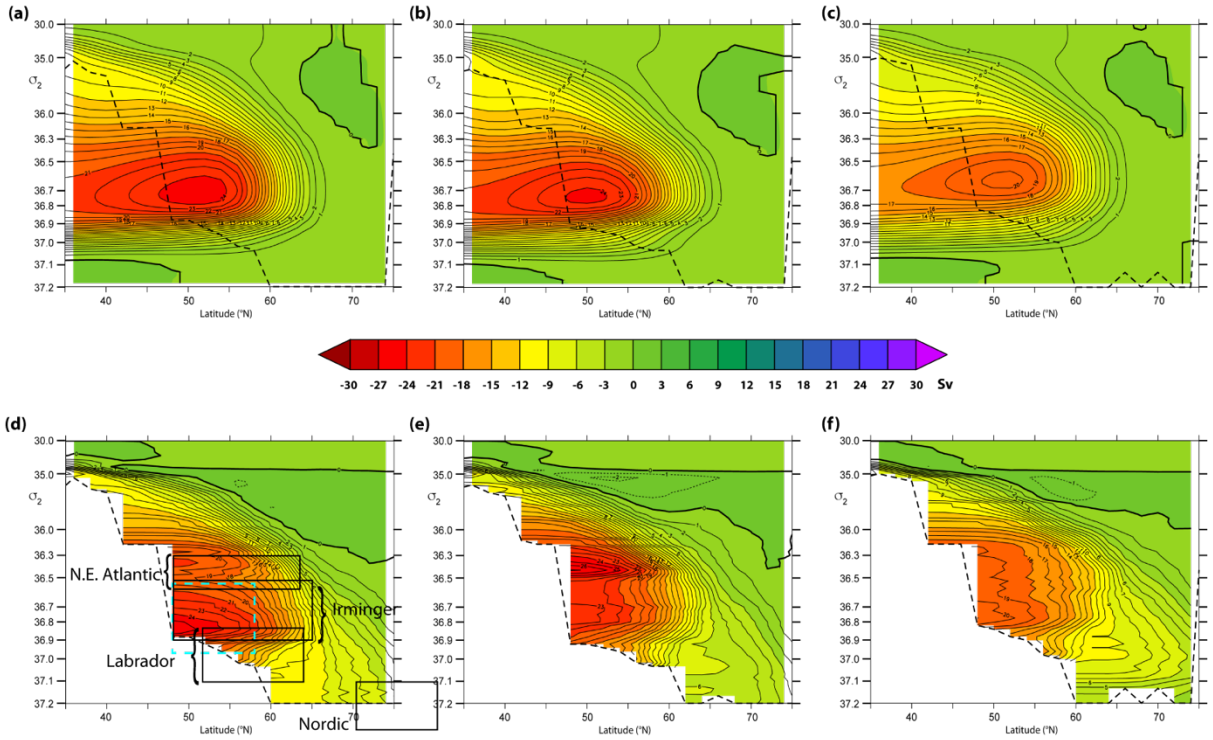

Figure 3. Mean Atlantic meridional overturning streamfunction in 1996-2005 in experiments forced with CORE2 (a); DFS5.2 (b) and JRA55 (c); and the surface forced streamfunction with CORE2 (d); DFS5.2 (e) and JRA55 (f). The dashed cyan box in panel (d) shows the region in density-latitude space over which the overturning metrics $T_{OV}(t)$ and $T_{SF}(t)$ will be evaluated, and the black boxes enclose the respective regions where deep convection occurs (see Figure 2).

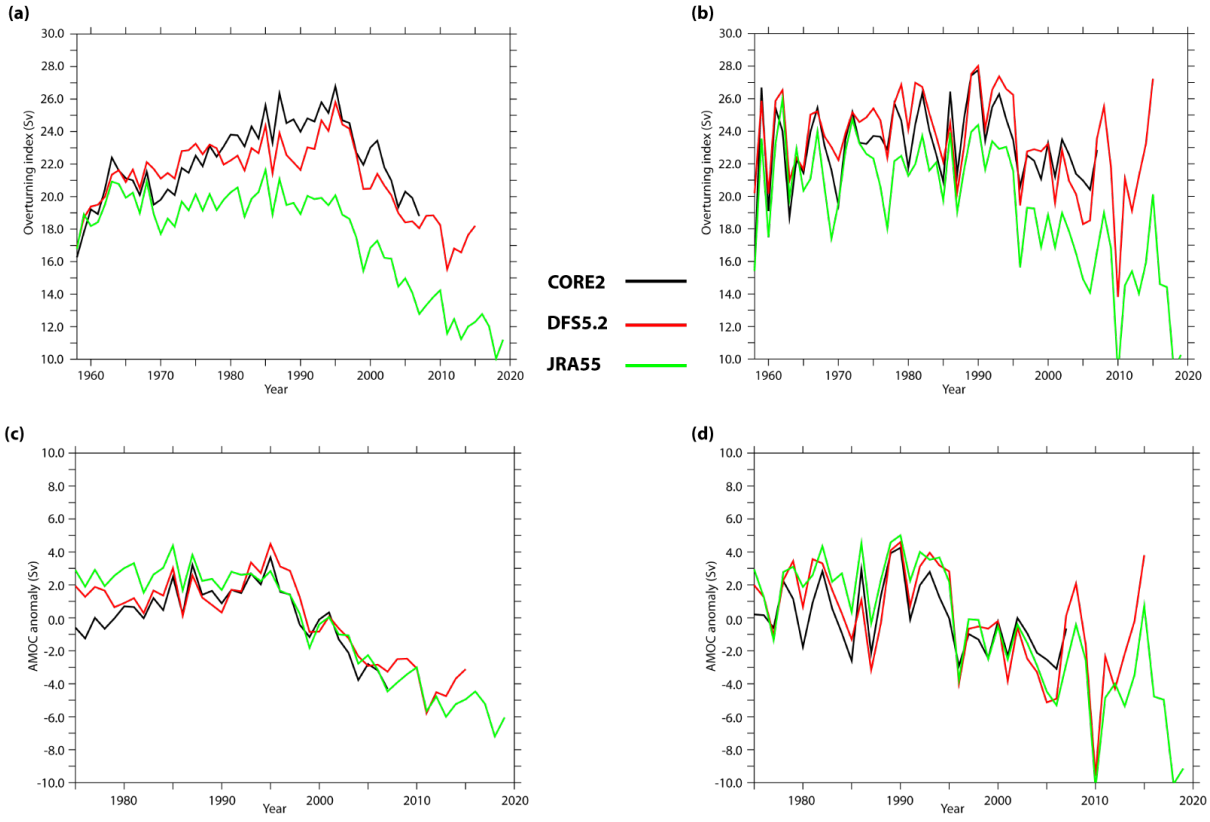

Figure 4. Time evolution of streamfunction indices for the three model integrations: (a) overturning strength; (b) surface-forced circulation; (c) anomaly of overturning index with respect to the respective mean from 1976 to 2005; and (d) anomaly of the surface-forced index with respect to the time mean from 1976 to 2005. Note the different scales on the x-axis between the upper and lower panels.

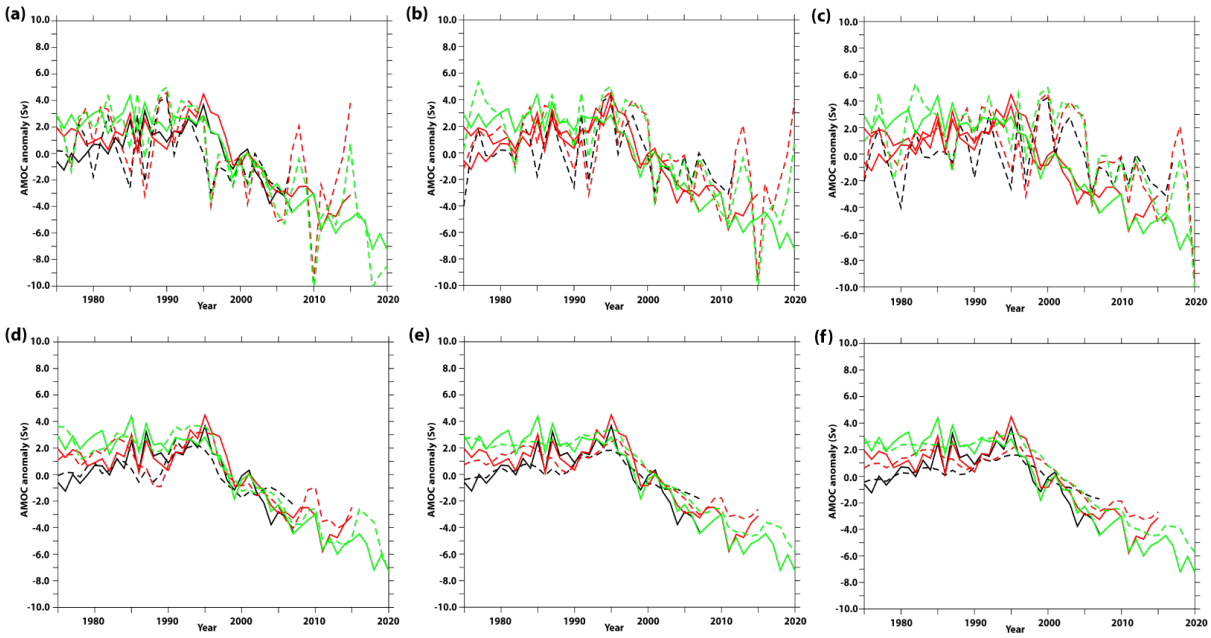

Figure 5. Overturning index T_{OV} (solid lines) with surface-forced index T_{SF} delayed by (a) 0 years; (b) 5; and (c) 10 years; and accumulated overturning indices (dashed lines) with surface-forced indices averaged over (d) the previous 5 years with constant weights; (e) the previous 10 years with ramped weights; and (f) the previous 15 years with ramped weights.

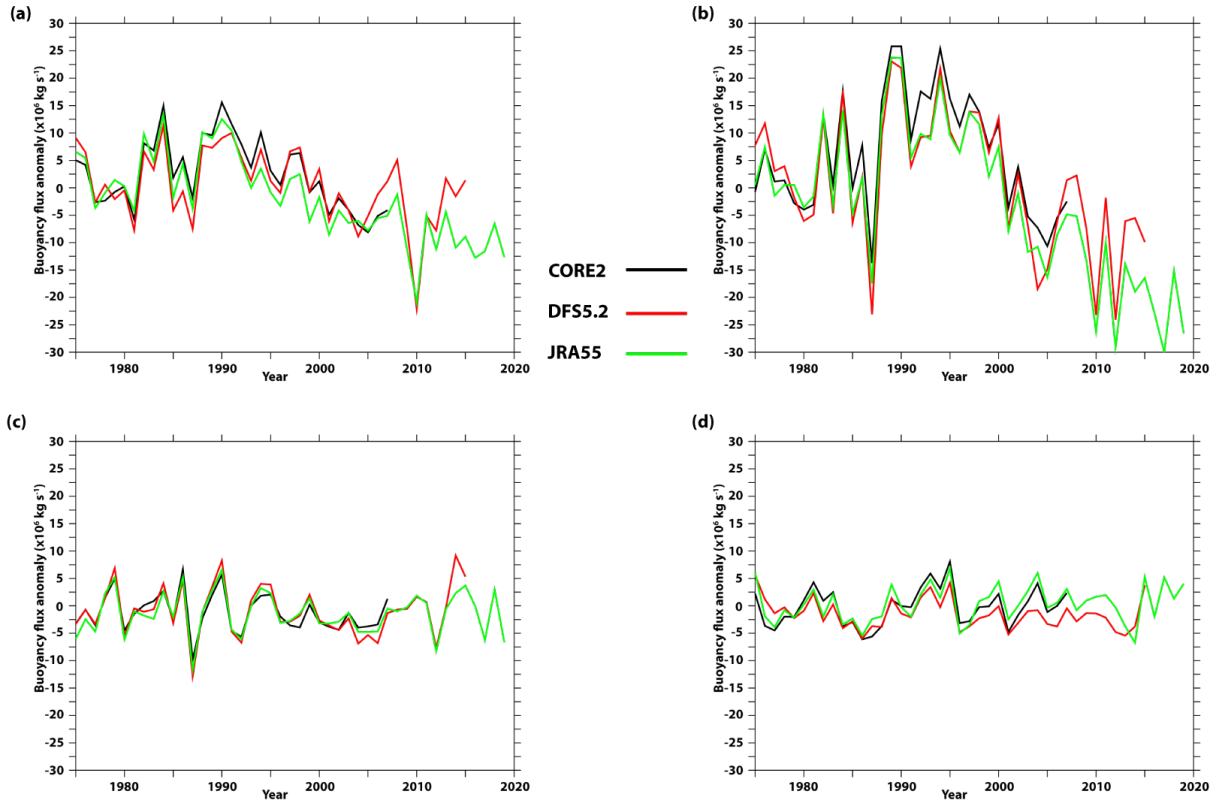

Figure 6. Wintertime (DJF) buoyancy loss anomalies (x10^6 kg s^{-1}) from annual mean heat flux, integrated over (a) the Labrador Sea; {b) the Irminger Sea; (c) the north-east Atlantic; and (d) the Nordic Seas in each experiment, with respect to the mean from 1976 to the end of the respective integration.

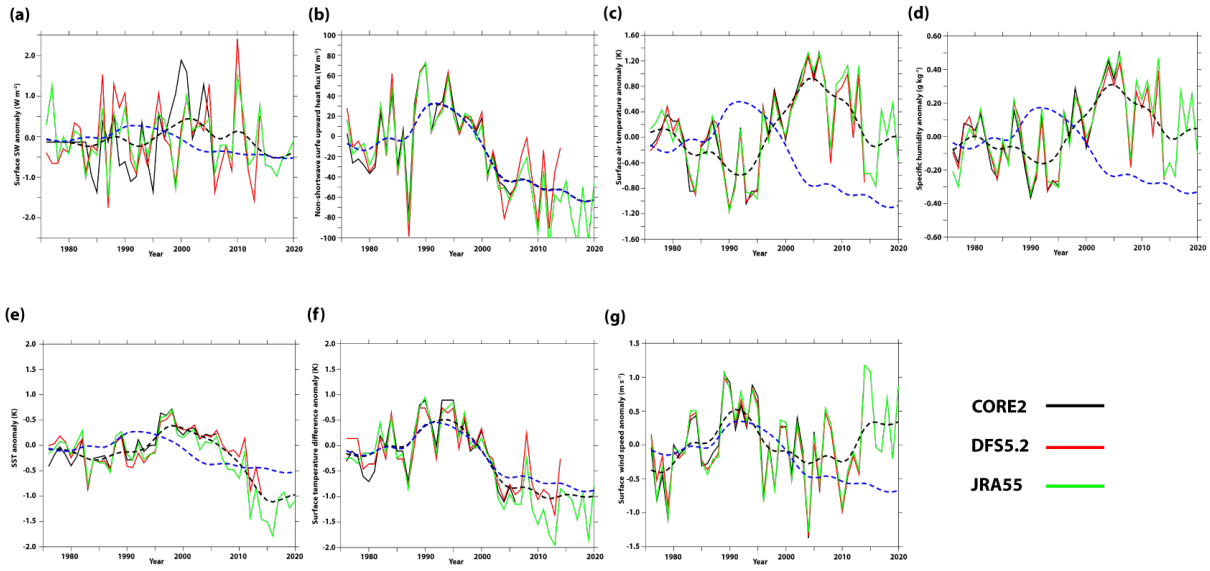

Figure 7. Wintertime (DJF) anomalies from the 1976-2005 means of surface fields averaged over the Irminger Sea from the experiments: (a) shortwave radiation; (b) Total upward heat flux minus the shortwave component; (c) near-surface air temperature; (d) near-surface specific humidity; (e) sea surface temperature; (f) sea surface temperature minus air temperature; and (g) the wind speed. The dashed black line on each panel is the ensemble mean over all the fields available in a given year, with a Gaussian windowed low-pass filter with half-width five years, for each quantity. The dashed blue lines show the upward winter surface heat flux anomaly, also low-pass filtered and normalised to have the same variance as the respective index, for comparison.

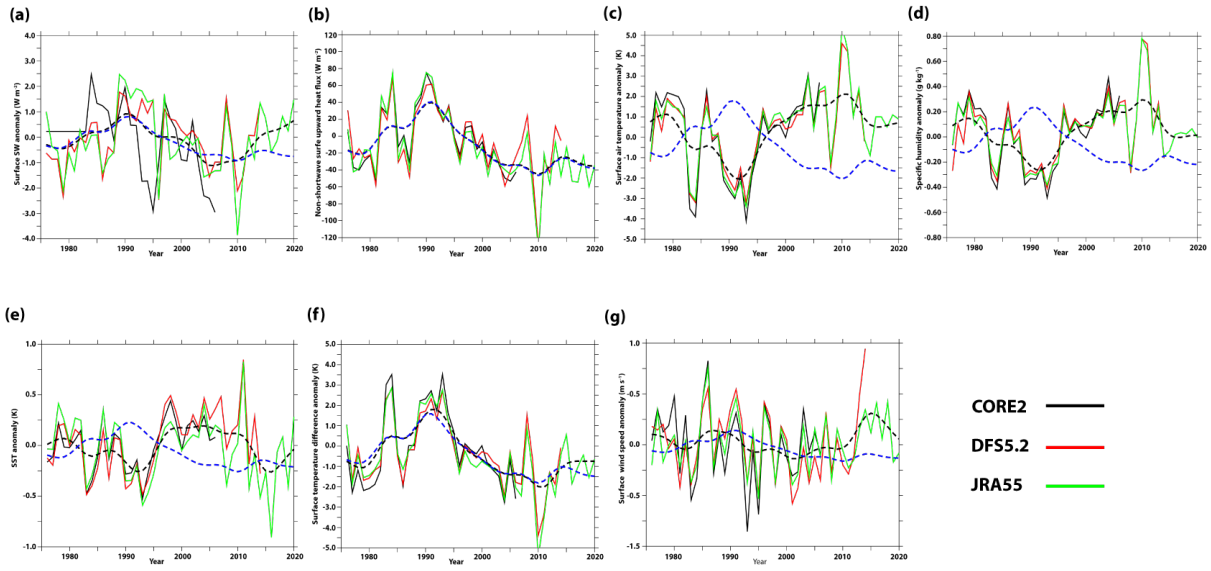

Figure 8. Wintertime (DJF) anomalies from the 1976-2005 means of surface fields averaged over the Labrador Sea from the experiments: (a) shortwave radiation; (b) Total upward heat flux minus shortwave component; (c) near-surface air temperature; (d) near-surface specific humidity; (e) sea surface temperature; (f) sea surface temperature minus air temperature; and (g) the wind speed. The dashed black line on each panel is the ensemble mean over all the fields available in a given year, with a Gaussian windowed low-pass filter with half-width five years, for each quantity. The dashed blue lines show the upward winter surface heat flux anomaly, also low-pass filtered and normalised to have the same variance as the respective index, for comparison.

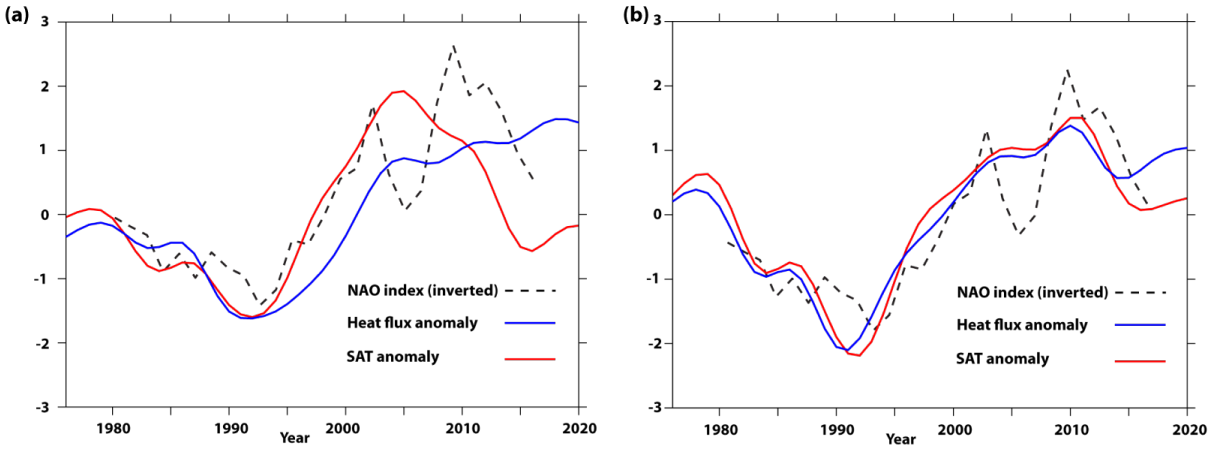

Figure 9. Normalised and low-pass filtered wintertime (DJF) anomalies of ensemble mean downward heat flux (blue line) and surface air temperature (red

line) averaged (a) over the Irminger Sea and (b) over the Labrador Sea; along with the NAO index from Robson et al. (2018), inverted for consistency (dashed black line).